Nanoscale

ROYAL SOCIETY OF CHEMISTRY

PAPER

View Article Online
View Journal | View Issue

Check for updates

Cite this: *Nanoscale*, 2023, **15**, 15994

Tuneable effects of pyrrolic N and pyridinic N on the enhanced field emission properties of nitrogen-doped graphene

Guodong Meng,*[a] Fuzhi Zhan,[a] Junyi She,[a] Jinan Xie,[a] Qinren Zheng,[a] Yonghong Cheng[a] and Zongyou Yin*[b]

Received 15th June 2023,
Accepted 14th September 2023

DOI: 10.1039/d3nr02861e

rsc.li/nanoscale

Graphene is one of the most potential field emission cathode materials and a lot of work has been carried out to demonstrate the effectiveness of nitrogen doping (N doping) for the enhancement of field emission properties of graphene. However, the effect of N doping on graphene field emission is lacking systematic and thorough understanding. In this study, undoped graphene and N-doped graphene were prepared and characterized for measurements, and the field emission property dependence of the doping content was investigated and the tuneable effect was discussed. For the undoped graphene, the turn-on field was 7.95 V μm^{-1} and the current density was 7.3 $\mu A\ cm^{-2}$, and for the 10 mg, 20 mg, and 30 mg N-doped graphene samples, the turn-on fields declined to 7.50 V μm^{-1}, 6.38 V μm^{-1}, and 7.28 V μm^{-1}, and current densities increased to 21.0 $\mu A\ cm^{-2}$, 42.6 $\mu A\ cm^{-2}$, and 13.2 $\mu A\ cm^{-2}$, respectively. Density functional theory (DFT) calculations revealed that N doping could bring about additional charge and then cause charge aggregation around the N atom. At the same time, it also lowered the work function, which further enhanced the field emission. The doping effect was determined by the content of the pyrrolic-type N and pyridinic-type N. Pyridinic-type N is more favourable for field emission because of its smaller work function, which is in good agreement with the experimental results. This study would be of great benefit to the understanding of N doping modulation for superior field emission properties.

Introduction

As the core component of vacuum electronic devices, carbon nanomaterials have been extensively studied for application in the electron emission cathode[1] owing to their excellent electrical and thermal conductivity, high-temperature resistance, and particle bombardment resistance.[2] Among them, the emerging two-dimensional material graphene is believed to be a very promising candidate for the electron emission sources because of its large surfaces and sharp edges.[3–7] Several methods, such as mechanical exfoliation and chemical reduction, have been reported for the preparation of graphene; however, these preparation processes have challenges, such as low yield, constrained control over the process, integration difficulties with electronics, and restricted customization of the materials. On the other hand, chemical vapor deposition (CVD) is an effective method to achieve larger-scale and lower-cost growth of graphene. However, the field emission properties of the graphene prepared by CVD are usually poor, and it is profoundly important to enhance the field emission properties of graphene prepared *via* CVD, especially in terms of understanding the underlying mechanisms driving its improvement.

In the past two decades, graphene field emitter has been continuously improved for enhancing the field emission properties through various ways, including structure optimization and material modification. One can find numerous graphene-based field emitters with different structures, such as vertically curved graphene,[8,9] graphene/carbon nanotube, graphene/ZnO, and graphene/nanoparticles.[10–12] For material modification, doping graphene with heteroatoms (boron, nitrogen, *etc.*) is a common way to tune the electronic and mechanical properties of graphene,[13,14] thus improving carrier mobility and decreasing the work function.[15–20]

Thus far, there have been a number of studies on N doping of graphene for the enhancement of field emission properties. Palnitkar *et al.* prepared undoped and N-doped graphene by arc discharge method and found that the N-doped graphene exhibited a lower turn-on field of 0.6 V μm^{-1} compared to undoped graphene of 0.8 V μm^{-1}.[15] Owing to N doping, the up-shift of the Fermi level can decrease the work function of

---

[a] *State Key Laboratory of Electrical Insulation and Power Equipment, Xi'an Jiaotong University, Xi'an 710049, China. E-mail: gdmengxjtu@xjtu.edu.cn*
[b] *Research School of Chemistry, The Australian National University, Canberra, Australian Capital Territory 2601, Australia. E-mail: zongyou.yin@anu.edu.au*

graphene. Therefore, the N-doped graphene emitter has better field emission properties. Kashid *et al*. compared the field emission of undoped with N-doped graphene by *in situ* transmission electron microscopy. Undoped and doped graphenes required voltages of 230 V and 110 V, respectively, to maintain the same field emission current.[16] The low turn-on voltage of N-doped graphene was explained using the improved conductivity and the up-shift of the Fermi energy level. Soin *et al*. prepared vertically curved undoped and N-doped graphenes by a microwave plasma-enhanced chemical vapor deposition method.[17] *In situ* nitrogen plasma treatment was carried out for doping and compared with undoped graphene, N-doped graphene showed significant improvement in field-emission characteristics by lowering the turn-on field from 1.94 to 1.0 V μm^{-1}. The enhancement can be attributed to the increase in the surface defects, shift of the Fermi level to higher binding energies, and reduction in the work function. Zhao *et al.* prepared graphene by microwave plasma-enhanced chemical vapor deposition, and N doping was realized by ammonia (NH_3) plasma treatment to enhance its field emission,[18] and Zheng achieved N doping facilitated by nitrogen microwave plasma.[19] Guo *et al.* heated the thin layers containing glucose and/or urea to grow N-doped vertical graphene, and the turn-on field dramatically reduced from 5.1 V μm^{-1} for glucose-derived graphene to 2.6 V μm^{-1} for the ones derived from glucose + urea. However, for the sample prepared using only urea, the turn-on field was higher than that of the sample derived from glucose + urea owing to the relatively poor crystallinity despite more N atoms were doped.[20]

To the best of our knowledge, these studies have demonstrated that doping can improve the field emission properties of graphene and most analyses simply attribute this to a reduction in the work function. Some studies have shown that the field emission of samples significantly degrades with a further increase in N doping, but we believe the reason is only that the poor crystallinity increased the disordered phase in the samples. Therefore, the effect of doping concentration on the field emission of graphene and the underlying mechanism demands a comprehensive and systematic understanding.

Herein, we present the tuneable effect of pyrrolic N and pyridinic N on the enhanced field emission properties of nitrogen-doped graphene. Graphene samples with different doping contents were prepared with various masses of urea as the nitrogen source using the CVD method, and the field-emission properties were measured. It was found that the field-emission properties of graphene reduce with the further increase in the urea addition. The specific values of the work function and energy levels of different doping types of graphene were calculated using the first principles to illustrate the influence mechanism of N doping. First-principles calculation results show that the work function of pyridinic nitrogen drops more than that of pyrrolic nitrogen. N doping in graphene benefits the field-emission properties of both the work function reduction and the charge aggregation effect. The degradation is due to the increases of the pyrrolic N and the impurity scattering effect. The conclusion of our study is different from previous studies in that the effect of N doping on the field emission properties of graphene was only attributed to the reduction of the work function by the introduction of nitrogen without considering the effect of different N doping contents and/or types.[21–24] Instead, it is believed that the effect is related to the different changes in the work function and energy level caused by different contents and types of N doping. Our study provides insight into the specific tuneable effect of different N doping configurations on field emission properties.

Experiments

Materials

Copper foil (25 μm thick, 99.99%) was purchased from Alfa Aesar Company Inc. (UK). Urea (99%) and methane (99.99%) were provided by Sinopharm Chemical Reagent Co., Ltd and Xi'an Feng Tereste Gas Co., Ltd, respectively, and were used for the preparation of undoped and N-doped graphenes.

Synthesis of undoped and N-doped graphene

In this study, undoped and N-doped graphenes were prepared using the CVD method using copper foil as the catalytic substrate.[25] The schematic diagram of the experimental setup is shown in Fig. 1(a). To remove surface impurities and oxides, a Cu foil was soaked in glacial acetic acid, acetone, isopropanol, and deionized water for 5 min. The processed Cu foil was placed in a quartz tube in the middle of the heating zone of the furnace and heated rapidly to 1030 °C for 30 min under the flow of Ar at 300 sccm. Then, 2 sccm CH_4 and 20 sccm H_2 were injected and undoped graphene was grown for 5 min. After the growth of graphene, the flow of H_2 and CH_4 was shut off as a cooling step. For the N-doped graphene, the preceding steps were the same as the undoped graphene preparation process, and the urea was heated to the setting value by a heating band while introducing CH_4. After the growth process, the furnace and heating band were cooled to room temperature.

The as-grown graphene was transferred from Cu foil onto a SiO_2/Si or the Si substrate using the polymethyl methacrylate (PMMA)-assisted wet method for further characterizations and measurements.[26]

Structure characterization

The morphology of undoped graphene and N-doped graphene was characterized using scanning electron microscopy (SEM, Gemini SEM 500), optical microscopy (OM, Olympus BX51), and atomic force microscopy (AFM; Bruker Dimension Icon). The microstructure of graphene was investigated using a Raman spectroscope (Renishaw inVia Qontor with an excitation wavelength of 514 nm). The chemical composition of graphene was analysed using energy-dispersive X-ray analysis (EDS) and X-ray photoelectron spectroscopy (XPS, Thermo Fisher ESCALAB Xi+). The work function of graphene was

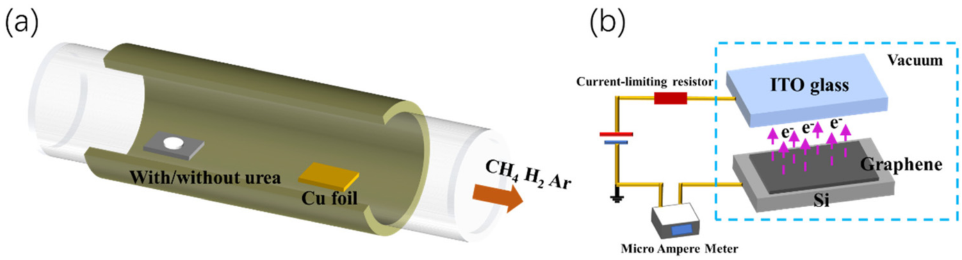

Fig. 1 (a) Schematic diagram of the experimental setup for graphene growth. (b) Schematic diagram of the experimental setup for field emission.

measured by Kelvin probe force microscopy (KPFM, Agilent 5500 atomic force microscope).

Field emission measurement

Field emission measurements were performed using a parallel plate-plate configuration in a chamber with a vacuum of 10^{-3} Pa. The schematic diagram of the experimental setup is shown in Fig. 1(b). The anode is an ITO glass, and the grown undoped or N-doped graphene serves as the cathode. Quartz glass was used as the supporting isolation part, and the electrode gap was determined from the thickness of the quartz glass. The electrode gap was fixed at 200 μm in this study. The voltage source adopted was using the HB-Z502 DC high-voltage power supply. The voltage value was measured using the LeCroy 104MXS-B oscilloscope and the current value was measured using a high-precision VC8901a multimeter with an accuracy of up to 0.01 μA.

DFT calculation

The first-principles calculations were performed based on the density functional theory (DFT) with generalized gradient approximation (GGA) in the form of Perdew–Burke–Ernzerhof (PBE) using the Dmol3 software.[25] Periodic boundary conditions (PBC) were employed to describe the 2D structure on the graphene surface. In this model, the 6 × 6 × 1 graphene supercell containing 61 carbon atoms was used and the graphene-based lattice parameters were a = 9.84 Å, b = 9.84 Å, c = 15 Å. The undoped graphene and N-doped graphene were optimized without any symmetry constraints. Double numerical basis sets, including polarization functions on all atoms (DNP), were used in the calculations.[27–29] The global cutoff radius was set to be 4.4 Å. The convergence criterion applied during geometry optimization was 1.0×10^{-5} Hartree for energy.

Results and discussion

Undoped graphene and the N-doped graphene with urea mass of 10 mg, 20 mg, and 30 mg were named PG, NG10, NG20, and NG30, respectively. Fig. 2(a)–(d) shows SEM images of PG and NG. PG shows a smoother surface than NG and there are some urea particles on the surface of NG, which are introduced by the carrier gas. Fig. 2(e) shows the OM image of the graphene

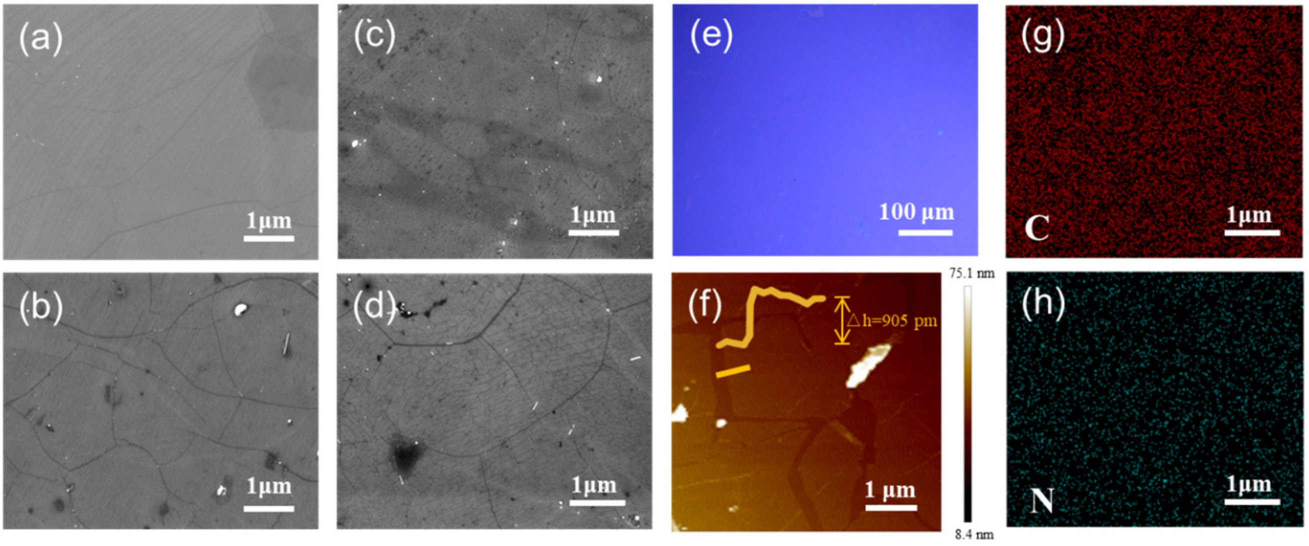

Fig. 2 Surface morphologies of graphene after transferring onto a SiO_2/Si substrate. SEM images of NG (a) pure (b) 10 mg (c) 20 mg (d) 30 mg. (e) Optical images. (f) AFM images. EDS elemental mapping images of (g) C (h) N.

after being transferred onto a SiO_2/Si substrate, which shows a clean, complete, and continuous film. Layers of graphene can be verified by the AFM measurement. The AFM image obtained in the contact mode at a RH of ~60%, as shown in Fig. 2(f), demonstrates that graphene is uniform with an apparent thickness of about 0.9 nm at the edge. It indicates that the as-grown graphene had a monolayer structure.[30] The components in the NG sample were confirmed by EDS mapping (Fig. 2(g and h)), which showed a uniform distribution of the signals of C and N, as expected.

The Raman analysis of PG and NG, using different weights of the urea, was performed to analyse the typical features of graphene. Fig. 3(a) presents the Raman spectrum, which shows the typical D band (1350 cm^{-1}), G band (1580 cm^{-1}), and 2D band (2680 cm^{-1}) peaks for PG and NG, and NG exhibited an additional characteristic peak at D′ band (1620 cm^{-1}).[31,32] As nitrogen atoms are doped into the graphene network, the D peak intensity increases rapidly with respect to undoped graphene. I_D/I_G (the intensity ratio of the D band to G band) shows the change from 0.09 to 1.42 for samples due to the decrease in crystallinity from N doping. Comparing NG with PG, we find that the 2D peak decreases with the increase in the amount of urea, and the weak 2D peak also indicates poor crystallinity/graphitization for the prepared NG. In addition to the peak intensity, the G band shows a redshift in NG, which is a sign of atomic insertions. The shift in the G band can be interpreted in terms of the size of the C–C ring and the changes in the electronic structure,[33] which indicates the enhancement of the N doping. The 2D peak shape of graphene is related to the number of graphene layers, and there was only one symmetric Lorentz curve for the 2D peak of single-layer graphene when Lorentz fitting was performed on it.[34] As seen in Fig. 3(b), the Lorentzian fit of 2D peaks of PG and NG has only one symmetric Lorentzian fit curve, which also indicates its monolayer structure.

To determine the chemical composition of PG and NG, XPS measurements were performed on the grown graphene, as shown in Fig. 3(c), in the energy region of 0–500 eV. As shown in Fig. 3(c), the peaks at 285 eV and 399 eV correspond to the elements C and N, confirming the existence of element N.[35,36] The C 1s peak at 285 eV was fitted by sub-peaks, and the results are shown in Fig. 3(d). Three sub-peaks at 284.5 eV, 285.6 eV, and 286.4 eV were obtained, corresponding to the SP^2-hybridized C–C bond, SP^2-hybridized C–N bond, and SP^3-hybridized C–N bond, respectively.[36] As can be seen from Fig. 3(d), with the increase in the amount of urea, the C–N peak appears and the intensity gradually increases. It demonstrated the successful doping of N into graphene. The proportion of doping types can be quantified by fitting the split peak to the N 1s peak at 399 eV. The positions of the corresponding peaks for pyridinic-type nitrogen, pyrrolic-type nitrogen, and graphite-type nitrogen are 398.5 eV, 400.5 eV, and 401.5 eV,[37] respectively. For NG10, with 87.2% and 12.8% of pyridinic N and pyrrolic N, respectively, the N binding configuration includes almost all pyridinic N. For NG30, the N binding configuration includes 50.3% pyridinic N and 49.7% pyrrolic N, as measured by fitting the curve of the N 1s peak (see Fig. 3(d)). The amount of pyrrolic N increases significantly, whereas that of pyridinic N species drops slightly and none of the graphite-type nitrogen was generated because pyridinic-type nitrogen and pyrrolic-type nitrogen have better thermal stability and are more likely to exist at the edges of the graphene lattice, which is consistent with the previous results of the first-principles calculations.[38,39] Therefore, pyridinic N and pyrrolic N doping might play an important role in regulating the electronic properties and enhancing the field emission properties of graphene.

The field-emission properties of PG and NG were investigated. Fig. 4(a) and (b) display the relationship between the emission current density(J) and the applied electric field strength (E) and the Flower–Nordheim (F–N) plotting of the emission data, which exhibits a liner behavior, indicating that the field emission of PG and NG was dominated by the tunnel effect. It can be seen from Fig. 4(a) that the turn-on E, defined at the current density of 1 μA cm^{-2}, was 7.95 V $μm^{-1}$ and the current density was 7.3 μA cm^{-2} of PG, which is comparable to the reported values for graphene films prepared by the CVD method, as shown in Table 1.[40–44] In general, the doping of nitrogen has an enhancing effect on the field emission properties of graphene. Interestingly, the enhancing effect is not linear, and it is optimal when the introduced urea mass is 20 mg, with a turn-on E of 6.38 V $μm^{-1}$ and a current density of 42.6 μA cm^{-2}. After that, the field emission properties decrease with the increase in the concentration of doped N.

To understand how the N doping configuration affects the field emission properties of graphene, first-principles calcu-

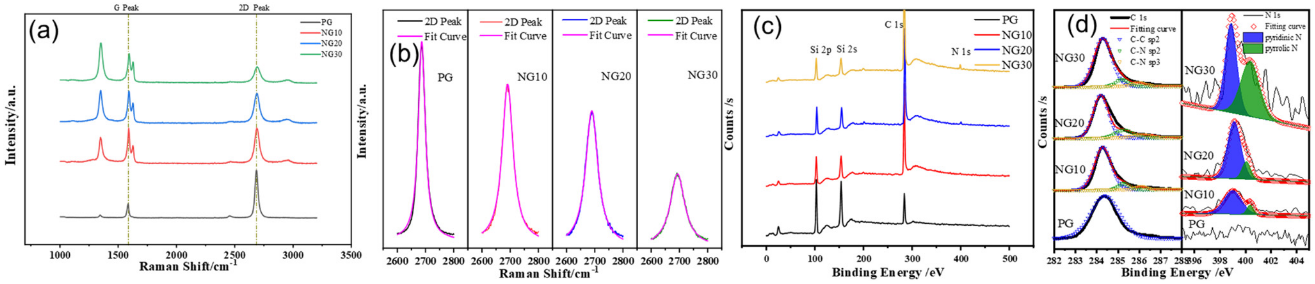

Fig. 3 (a) Raman spectrum. (b) Lorentz-fitted split-plot of the 2D peak. (c) XPS spectra survey. (d) Split-peak fitting of C 1s and N 1s.

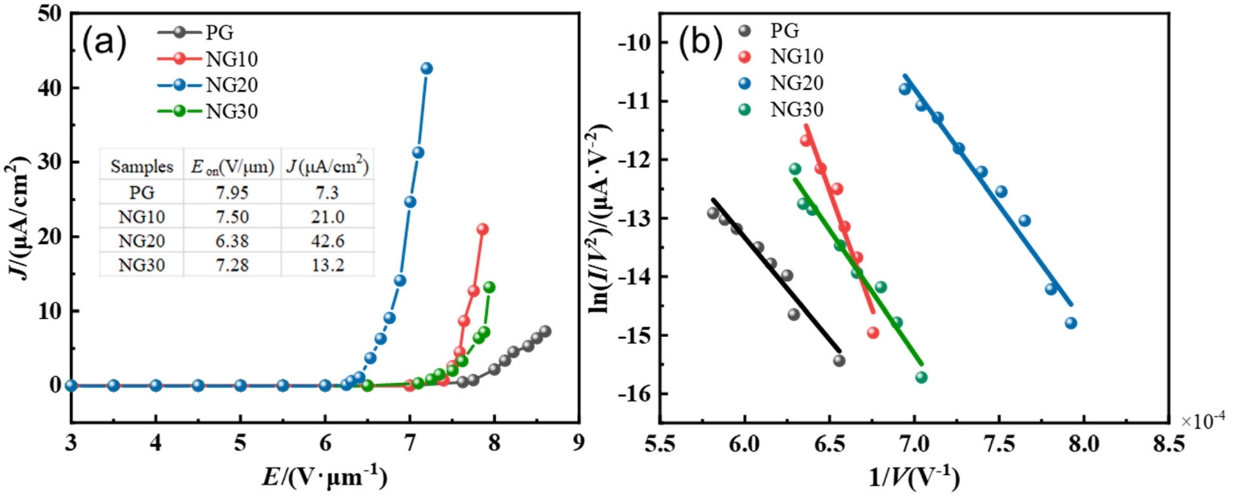

Samples	E_{on}(V/μm)	J(μA/cm^2)
PG	7.95	7.3
NG10	7.50	21.0
NG20	6.38	42.6
NG30	7.28	13.2

Fig. 4 Field-emission properties of PG and NG. (a) *J*–*E* curves. (b) Fowler–Nordheim plot of data in (a).

Table 1 List of field-emission properties of graphene grown by thermal CVD

Ref.	Turn-on E (V μm^{-1})	J (μA cm^{-2})
40	9.04	40.2
41	32	150
42	4.4	5
43	7	140
44	14	9
This work	6.38	42.6

lations were performed in this study to provide accurate values of the work function, energy levels, and charge distribution at the dopant sites of PG and NG. The optimized structures of PG and NG are shown in Fig. 5(a). The pyridinic NG structure contains three pyridinic N atoms (N1, N2, and N3), and the pyrrolic NG structure contains two pyridinic N atoms (N1 and N2) and one pyrrolic N atom (N3). In other words, the carbon atoms around the vacancy defect site in graphene are replaced by N atoms to form pyridinic N.[45–47] The substitution of all carbon atoms around a vacancy defect with pyridinic N atoms can greatly decrease the formation energy of defective graphene, mainly due to the vanishing of dangling bonds in these systems.[48,49] Therefore, the model we have used is expected to be the dominant structure compared with other possible configurations.

Fig. 5(b) shows that the band gaps of pyridinic NG and pyrrolic NG are 1.7 eV and 1.3 eV, respectively. The HOMO values for pyridinic NG and pyrrolic NG are almost equal, while the LUMO of pyridinic NG is closer to the vacuum level, making its Fermi level closer to the vacuum level. Therefore, the work

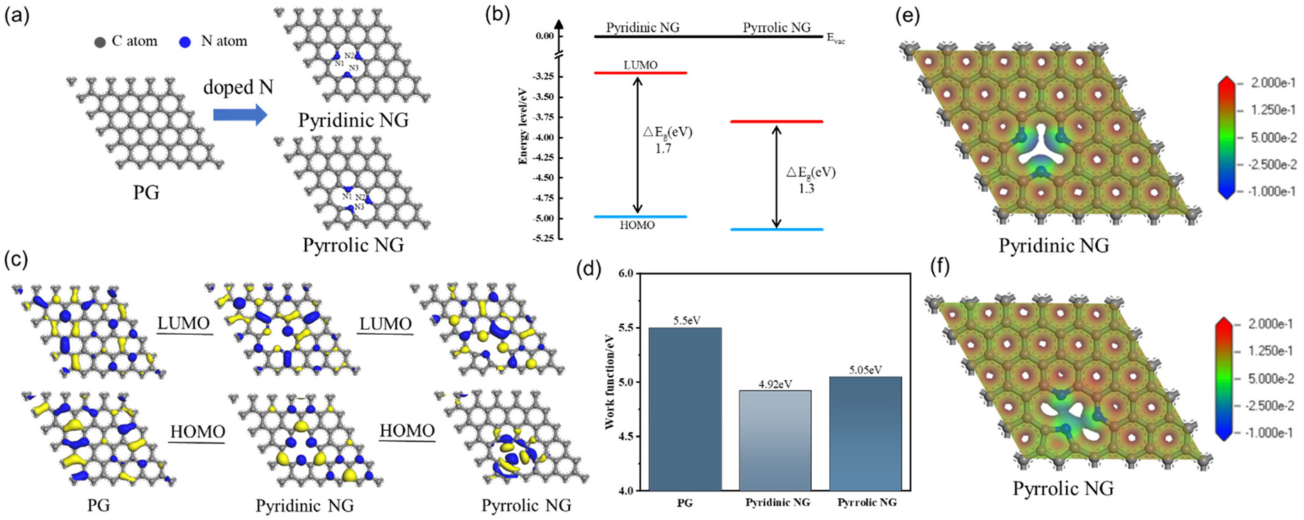

Fig. 5 (a) Atomic structure models, (b) energy levels, (c) local electron density distributions, (d) work function, and (e and f) the calculated Hartree potential analysis of the pyridinic NG and pyrrolic NG.

function of pyridinic NG is lower than that of pyrrolic NG. The work function is 5.50 eV for PG, 4.92 eV for pyridinic NG, and 5.05 eV for pyrrolic NG, as shown in Fig. 5(d). In conclusion, pyridinic NG is more beneficial to the improvement of field emission properties than pyrrolic NG.

A significant change in the electron density of the LUMO of NG was observed, as shown in Fig. 5(c). For PG, both HOMO and LUMO are uniformly localized on the graphene surface. However, the LUMO and HOMO states of NG are shifted to the "inside" of graphene near the nitrogen atom. The LUMO state in the "inside" of graphene is a localized state,[50] and when the electric field is applied, the localized state will be filled with the electrons transferred from other states, and then these electrons will be excited to vacuum.[22] Thus, the LUMO states play a very important role in the field emission process. Therefore, the introduction of nitrogen atoms may provide new electron emission sites and the electrons could be emitted from the electron emission sites provided by nitrogen atoms after the electrons are pumped from the HOMO to LUMO.

Fig. 5(e and f) shows the charge distribution at the dopant sites of pyridinic NG and pyrrolic NG. The presence of a negative net charge on nitrogen dopants is evident from the calculated Hartree potential (Fig. 5(e and f)), implying that the N doping could promote charge aggregation at the doping position. As the electric field increases, electron aggregation becomes more active and these electrons will fill the empty level of the conduction band, which can effectively lower the field emission barrier and make the electrons more easily excited into the vacuum, leading to the enhancement of the field emission properties. The net charge on the nitrogen dopant comes from the donation of electrons and the subsequent electron redistribution of the graphene pi-band.[51]

To illustrate the accuracy of the calculated results, the work function of the graphene sample was measured using KPFM. A series of KPFM images of the graphene samples is shown in Fig. 6. The contact potential difference (CPD) can be obtained from the contact potential maps, as shown in Fig. 6(i). Since the CPD is generally interpreted as the difference in the work function between the tip and the sample surface,[52] once the work function of the tip is determined, the work function of graphene, $W_{\mathrm{F,g}}$, can be estimated using the equation, CPD = $W_{\mathrm{F,tip}} - W_{\mathrm{F,g}}$. Before measuring the graphene system, the work function of the tip was calibrated by taking the CPD on the HOPG. The work function of the HOPG is about 5.5 eV and the measured CPD value was almost −1200 mV so the tip work function is about 4.3 eV within the error of measurement. Therefore, the KPFM results demonstrate a decrease in the work function of N-doped graphene, ranging from 4.9 eV (pristine) to 4.5 eV. The work function of the pristine sample of ~4.9 eV is a reasonable value, compared with previously reported values.[53,54] It can be also seen that the degree of reduction in the work function decreases when the amount of urea increases from 20 to 30 mg (about 0.05 eV), which is consistent with the calculated results, indicating that the reduction in the work function is less pronounced for pyrrolic-type nitrogen.

Experimental results from XPS analysis suggest that as the N doping concentration increases, the type of N doping inside the graphene lattice changes accordingly. Therefore, the effects of different N doping concentrations and types on the field emission properties of graphene need to be considered. With the increase of doping N atoms, the graphene lattice is mainly in the form of pyridinic nitrogen at first, which can regulate its work function and energy level and benefit the field emission enhancement. Then, the amount of pyrrolic N species increases significantly, while those of pyridinic N species drop slightly, and the work function and energy level correspondingly change to the detriment of field emission. In addition, the impurity scattering effect of the increased nitrogen atoms also needs to be considered.[55] As the introduction of nitrogen atoms leads to the existence of lattice defects, such as vacancies and topology in graphene, electrons will be scattered by vibrating atoms and various lattice defects during the internal transport process, and the electrons will have less energy at the same applied voltage, which means that the impurity scattering effect will decrease the field emission elec-

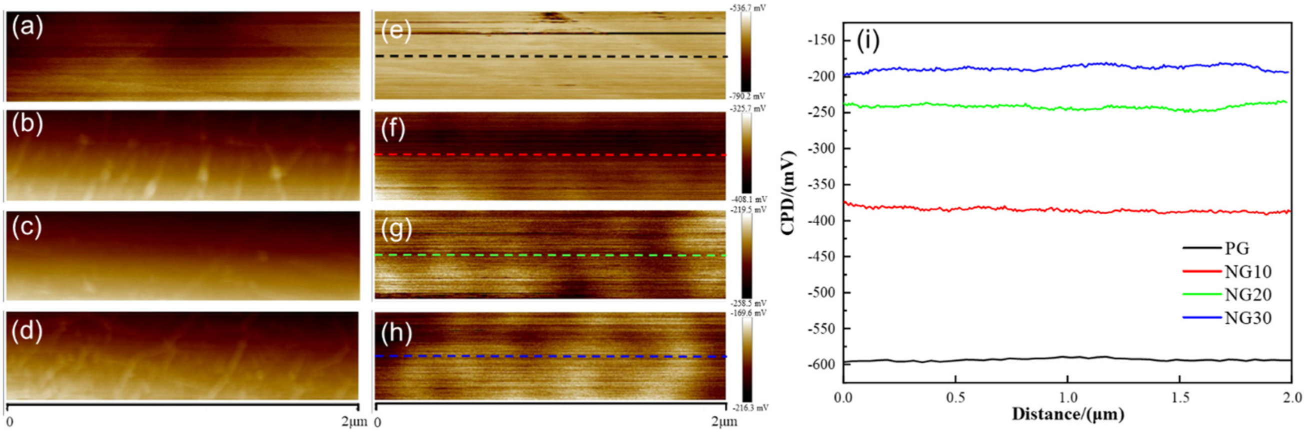

Fig. 6 (a–d) Topography, (e–h) contact potential maps, and (i) CPD of PG, NG10, NG20, and NG30 using KPFM.

tron tunneling probability. If the effect of the impurity scattering is greater than the enhancement of electron concentration brought about by nitrogen atoms, the field emission performance will be reduced. Therefore, the influence mechanism of N doping is mainly attributed to the following aspects: (1) N doping could lower the band gap and work function and aggregate charge, achieving enhanced field emission properties. (2) Pyridinic N shows better field-emission enhancement capability than pyrrolic N, and pyrrolic N increases significantly with the increase of doping N atoms. At the same time, the impurity scattering effect due to the increase in nitrogen atoms should be considered. Therefore, field emission properties of NG degrade with increasing urea addition.

Conclusions

The synthesis of undoped and N-doped graphenes by chemical vapor deposition is reported and the tuneable effect of pyrrolic N and pyridinic N on the enhanced field emission properties of nitrogen-doped graphene was studied. N doping could enhance the field emission properties of graphene with a declining turn-on field from 7.95 V μm^{-1} to 6.38 V μm^{-1} and a significant increase in the current density from 7.3 $\mu A\ cm^{-2}$ to 42.6 $\mu A\ cm^{-2}$. DFT calculations proved that on the one hand, the N doping could bring about the additional charge and cause charge aggregation around the N atom, which provides more emission sites. On the other hand, N doping could also lower the work function, which further enhances the field emission. Specifically, the doping effect was determined by the content of the pyrrolic-type N and pyridinic-type N. The work function of pyridinic-type N was calculated to 4.92 eV, smaller than that of the pyrrolic-type N (5.05 eV), which is more favourable for field emission, so the doping content should be carefully modulated to introduce a higher ratio of pyridinic-type N as well as a lower impurity scattering effect, which is in a good agreement with the experimental results. This study can provide insight into the modulation of N doping for better field emission properties. Future study will focus on the optimization of the proportion of pyridinic N graphene and the amount of N doping for superior field-emission properties.

Author contributions

Fuzhi Zhan performed the investigation and calculations, analysed the data. Guodong Meng and Fuzhi Zhan drafted the manuscript. Junyi She, Jinan Xie and Qinren Zheng assisted in the inspection of data. Guodong Meng, Yonghong Cheng, and Zongyou Yin designed the research, supervised the project, and analysed data. All authors have discussed and revised the manuscript.

Conflicts of interest

There are no conflicts to declare.

Acknowledgements

This work was supported by the National Natural Science Foundation of China (51977169). The authors thank Zijun Ren and Chenyu Liang at the Instrument Analysis Center of Xi'an Jiaotong University for their assistance with SEM and XPS analysis, respectively.

References

1 B. J. Yang, J. T. Chen, X. N. Wu, B. Liu, L. Y. Liu, Y. Tang and X. B. Yan, *Nanoscale*, 2021, **13**, 7622–7629.

2 K. S. Novoselov, A. K. Geim, S. V. Morozov, D. Jiang, Y. Zhang, S. V. Dubonos, I. V. Grigorieva and A. A. Firsov, *Science*, 2004, **306**, 666–669.

3 Y. L. Gao and S. Okada, *Carbon*, 2020, **157**, 33–39.

4 K. Sun, D. F. Diao, L. Yang, W. Q. Zhang and X. Fan, *Thin Solid Films*, 2018, **664**, 124–129.

5 D. A. Katzmarek, A. Pradeepkumar, R. W. Ziolkowski and F. Iacopi, *2D Mater.*, 2022, **9**, 022002.

6 C. Tsakonas, M. Dimitropoulos, A. C. Manikas and C. Galiotis, *Nanoscale*, 2021, **13**, 3346–3373.

7 S. Tang, Y. Zhang, P. Zhao, R. Z. Zhan, J. Chen and S. Z. Deng, *Nanoscale*, 2021, **13**, 5234–5242.

8 S. C. Xu, S. S. Wang, Z. Chen, Y. Y. Sun, Z. F. Gao, H. Zhang and J. Zhang, *Adv. Funct. Mater.*, 2020, **30**, 2003302.

9 S. C. Xu and J. Zhang, *Small Struct.*, 2020, **1**, 2000034.

10 J. Luo, L. Liu, F. Sun, X. Y. Tang, R. T. Zheng, X. L. Wu and G. A. Cheng, *Diamond Relat. Mater.*, 2020, **106**, 107848.

11 J. J. Yang, S. S. Shao, Y. X. Li, Y. H. Wang and C. Feng, *Front. Phys.*, 2021, **8**, 610510.

12 Y. Long, B. Zeng, J. L. Liu, Y. Yang, N. N. Li and Z. Wu, *J. Vac. Sci. Technol., B: Nanotechnol. Microelectron.: Mater., Process., Meas., Phenom.*, 2015, **33**, 012204.

13 X. L. Zou, L. Q. Wang and B. I. Yakobson, *Nanoscale*, 2018, **10**, 1129–1134.

14 K. J. Sankaran, M. Ficek, S. Kunuku, K. Panda, C. J. Yeh, J. Y. Park, M. Sawczak, P. P. Michalowski, K. C. Leou, R. Bogdanowicz, I. Lin and K. Haenen, *Nanoscale*, 2018, **10**, 1345–1355.

15 U. A. Palnitkar, R. V. Kashid, M. A. More, D. S. Joag, L. S. Panchakarla and C. N. R. Rao, *Appl. Phys. Lett.*, 2010, **97**, 063102.

16 R. V. Kashid, M. Z. Yusop, C. Takahashi, G. Kalita, L. S. Panchakarla, D. S. Joag, M. A. More and M. Tanemura, *J. Appl. Phys*, 2013, **113**, 214311.

17 N. Soin, S. S. Roy, S. Roy, K. S. Hazra, D. S. Misra, T. H. Lim, C. J. Hetherington and J. A. McLaughlin, *J. Phys. Chem. C*, 2011, **115**, 5366–5372.

18 C. X. Zhao, Y. Zhang, S. Z. Deng, N. S. Xu and J. Chen, *J. Alloys Compd.*, 2016, **672**, 433–439.

19 H. Zheng, Q. Q. Chu, P. Zheng, L. Zheng, X. L. Zheng, L. H. Shuo, F. M. Wu, Z. T. Wu, Y. Jiang and Y. Zhang, *J. Phys. Chem. C*, 2020, **124**, 21684–21691.

20 X. Guo, Y. Li, Y. Ding, Q. Chen and J. Li, *Mater. Des.*, 2019, **162**, 293–299.

21 G. Song, S. Luo, J. Zhang, M. Zhang, G. Qiu, A. Meng, Y. Lin and Z. Li, *J. Alloys Compd.*, 2020, **829**, 154411.

22 S. X. Yu, R. J. Tang, K. Zhang, S. Y. Wu and Z. Sun, *Vacuum*, 2019, **168**, 108817.

23 J. Gong, H. Y. Yang and P. Yang, *Composites, Part B*, 2015, **75**, 250–255.

24 W. J. Huang, W. J. Qian, H. J. Luo, M. L. Dong, H. Z. Shao, Y. W. Chen, X. Z. Liu and C. K. Dong, *Vacuum*, 2022, **198**, 110900.

25 X. L. Wang, Q. H. Yuan, J. Li and F. Ding, *Nanoscale*, 2017, **9**, 11584–11589.

26 F. Qing, Y. F. Zhang, Y. T. Niu, R. Stehle, Y. F. Chen and X. S. Li, *Nanoscale*, 2020, **12**, 10890–10911.

27 B. Delley, *J. Chem. Phys.*, 1990, **92**, 508–517.

28 B. Delley, *J. Phys. Chem. C*, 1996, **100**, 6107–6110.

29 B. Delley, *J. Chem. Phys.*, 2000, **113**, 7756–7764.

30 H. Lee and J. Y. Park, *Rev. Sci. Instrum.*, 2019, **90**, 103702.

31 M. Losurdo, M. M. Giangregorio, P. Capezzutoa and G. Brunoa, *Phys. Chem. Chem. Phys.*, 2011, **13**, 20836–20843.

32 E. S. Henriette, *Carbon*, 2004, **42**, 1713–1721.

33 A. Das, S. Pisana, B. Chakraborty, S. Piscanec, S. K. Saha, U. V. Waghmare, K. S. Novoselov, H. R. Krishnamurthy, A. K. Geim, A. C. Ferrari and A. K. Sood, *Nat. Nanotechnol.*, 2008, **3**, 210–215.

34 D. Graf, F. Molitor, K. Ensslin, C. Stampfer, A. Jungen, C. Hierold and L. Wirtz, *Nano Lett.*, 2007, **7**, 238–242.

35 L. M. Dai, *Nat. Energy*, 2016, **1**, 16041.

36 X. Wang, X. Li, L. Zhang, Y. Yoon, P. K. Weber, H. Wang, J. Guo and H. Dai, *Science*, 2009, **324**, 768–771.

37 D. Wei, Y. Liu, Y. Wang, H. Zhang, L. Huang and G. Yu, S, *Nano Lett.*, 2009, **9**, 1752–1758.

38 Y. F. Li, Z. Zhou, P. W. Shen and Z. F. Chen, *ACS Nano*, 2009, **3**, 1952–1958.

39 S. Y. Bu, N. Yao, M. A. Hunter, D. J. Searles and Q. H. Yuan, *npj Comput. Mater.*, 2020, **6**, 128.

40 Z. C. Yang, Q. Zhao, Y. X. Ou, W. Wang, H. Li and D. P. Yua, *Appl. Phys. Lett.*, 2012, **101**, 173107.

41 B. Mazurek, W. Mielcarek, J. Warycha, K. Prociow and J. Chmielowiec, *IEEE Trans. Dielectr. Electr. Insul.*, 2015, **22**, 3498–3503.

42 S. K. Behura, S. Nayak, Q. Q. Yang, A. Hirose and O. Jani, *J. Nanosci. Nanotechnol.*, 2016, **16**, 287–295.

43 J. J. Yang, S. S. Shao, Y. X. Li, Y. H. Wang and C. Feng, *Front. Phys.*, 2021, **8**, 610510.

44 G. L. Cheng, J. J. Yang, S. Quan, J. Zhong and J. S. Yu, *Chin. Vac. Sci. Technol.*, 2022, **4**, 290–294.

45 C. C. Ma, X. H. Shao and D. P. Cao, *J. Mater. Chem.*, 2012, **22**, 8911–8915.

46 R. E. Ambrusi and M. E. Pronsato, *Appl. Surf. Sci.*, 2019, **464**, 243–254.

47 M. Ivana, A. Katertna, B. S. Matthew, J. D. Michael, P. Svitlana and A. Plamen, *J. Phys. Chem. C*, 2016, **51**, 29225–29232.

48 M. D. Esrafili and B. Nejadebrahimi, *Appl. Surf. Sci.*, 2019, **475**, 363–371.

49 X. Liu, Y. Sui, T. Duan, C. Meng and Y. Han, *Catal. Sci. Technol.*, 2015, **5**, 1658–1667.

50 S. L. Zhang, Y. H. Zhang, S. P. Huang, H. Liu, P. Wang and H. Tian, *J. Phys. Chem. C*, 2010, **114**, 19284–19288.

51 B. Mallada, S. Y. Edalatmanesh, P. L. J. Redondo, A. Gallardo, R. Zboril, P. Jelinek, M. Svec and B. Torre, *ACS Sustainable Chem. Eng.*, 2020, **8**, 3437–3444.

52 J. H. Kim, J. H. Hwang, J. Suh, S. Tongay, S. Kwon, C. C. Hwang, J. Q. Wu and J. Y. Park, *Appl. Phys. Lett.*, 2013, **103**, 171604.

53 S. Ryu, L. Liu, S. Berciaud, Y. J. Yu, H. T. Liu, P. Kim, G. W. Flynn and L. E. Brus, *Nano Lett.*, 2010, **10**, 4944–4951.

54 Y. J. Yu, Y. Zhao, S. Ryu, L. E. Brus, K. S. Kim and P. Kim, *Nano Lett.*, 2009, **9**, 3430–3434.

55 R. Z. Wang and H. Yan, *J. Beijing Univ. Iron Steel Technol.*, 2020, **10**, 1081–1090.